Arch. Metall. Mater. **63** (2018), 4, 1805-1813

DOI: 10.24425/amm.2018.125108

Q. YUAN, G. XU*#, S. LIU*, M. LIU*, H. HU*

EFFECT OF STRAIN RATE ON THE MICROSTRUCTURE OF WARM-DEFORMED ULTRAFINED MEDIUM-CARBON STEEL

In this study, medium-carbon steel was subjected to warm deformation experiments on a Gleeble 3500 thermosimulator machine at temperatures of 550°C and 650°C and strain rates of 0.001 s^{-1} to 1 s^{-1}. The warm deformation behavior of martensite and the effects of strain rate on the microstructure of ultrafine grained medium-carbon steel were investigated. The precipitation behavior of Fe_3C during deformation was analyzed and the results showed that recrystallization occurred at a low strain rate. The average ultrafine ferrite grains of 500 ± 58 nm were fabricated at 550°C and a strain rate of 0.001 s^{-1}. In addition, the size of Fe_3C particles in the ferrite grains did not show any apparent change, while that of the Fe_3C particles at the grain boundaries was mainly affected by the deformation temperature. The size of Fe_3C particles increased with the increasing deformation temperature, while the strain rate had no significant effect on Fe_3C particles. Moreover, the grain size of recrystallized ferrite decreased with an increase in the strain rate. The effects of the strain rate on the grain size of recrystallized ferrite depended on the deformation temperature and the strain rate had a prominent effect on the grain size at 550°C deformation temperature. Finally, the deformation resistance apparently decreased at 550°C and strain rate of 1 s^{-1} due to the maximum adiabatic heating in the material.

Keywords: warm deformation; medium-carbon steel; ultrafine grain; strain rate; Fe_3C

1. Introduction

Grain refinement improves the strength of coarse-grained steels. Inexpensive alloying elements are added to ultrafine grained steels to save alloying resources and reduce the production cost of high strength steels. Therefore, ultrafine grained steels are low-cost alternatives in various engineering fields [1]. There are two main methods for the production of the ultrafine-grained steels. The first one is severe plastic deformation (SPD) that includes equal-channel angular pressing (ECAP) [2-4], accumulative roll bonding (ARB) [5-7], mechanical milling (MM) [8,9], and high-pressure torsion (HPT) [10,11]. These methods usually require a large equivalent plastic strain of more than four, which is harmful to the rolling equipment due to a high load. The other includes the advanced thermomechanically controlled processes (TMCP), among which cold rolling and annealing of a martensitic starting microstructure proposed by Tsuji et al. is effective in fabricating ultrafine low-carbon steel with a small accumulated strain [12,13]. Many investigations on the cold deformation of low-carbon martensite starting structure and subsequent annealing process have been conducted. However, the cold rolling martensite starting structure in medium-carbon steel cannot be obtained because of the low-temperature brittleness and relative ultrahigh hardness of medium-carbon martensite [14,15]. Therefore, warm compression has been utilized to fabricate ultrafine grains in medium-carbon steels. Hase et al. [16] studied the effect of initial microstructure on ultrafine grain formation in medium-carbon steels by warm deformation, and reported that ultrafine equiaxed ferrite grains with a mean diameter of 500 nm were formed by dynamic recrystallization with the initial microstructure of lath martensite. The effect of warm deformation on the microstructure and the mechanical properties of medium-carbon steel were analyzed by Li et al. [17]. They reported that the ultrafine grain microstructure was composed of submicron ferrite grains and nano-scale Fe_3C particles. Zhao et al. [15] focused on the microstructural evolution under warm compression of quenched medium-carbon steel. In addition, the fatigue behavior of ultrafine-grained medium-carbon steel was investigated by Ruffing et al. [18]. Fractography revealed different crack initiation sites like pre cracks and shear bands resulting from fisheye fractures initiated from non-metallic inclusions.

Ferrite + pearlite, ferrite + cementite and upper bainite are also used as the initial microstructures for the fabrication of ultra-fined medium-carbon steel [16]. There are only a few investigations have been performed so far on the fabrication of ultra-fined medium-carbon steel by warm deformation of martensite. Furthermore, in contrast to the studies on the fabrication of ultrafine medium-carbon steel by warm deformation of martensite, the effect of strain rate on the microstructure of ultrafine grained medium-carbon steel is rather less studied and almost there has been no attention paid on the precipitation behavior of Fe_3C at different strain rates during warm deformation of

* WUHAN UNIVERSITY OF SCIENCE AND TECHNOLOGY, THE STATE KEY LABORATORY OF REFRACTORIES AND METALLURGY; HUBEI COLLABORATIVE INNOVATION CENTER FOR ADVANCED STEELS, 947 HEPING AVENUE, QINGSHAN DISTRICT, WUHAN 430081, HUBEI, CHINA

Corresponding author: xuguang@wust.edu.cn

martensite. Therefore, the aim of the current work was to investigate the warm deformation behavior of martensite at different strain rates and the effect of strain rate on the microstructure of ultrafine grained medium-carbon steel. In addition, the constitutive equation of medium-carbon martensite was established. The outcome of this study would be useful in fabricating ultrafine grained medium-carbon steel and optimizing the warm processing technology of medium-carbon steels.

2. Experimental procedure

The experimental material with the chemical composition of Fe-0.44C-0.24Si-0.60Mn-0.02P-0.06S-0.02Als (wt.%) was taken from a hot strip plant. Cylindrical specimens with the dimensions of φ 6 mm × 12 mm, corresponding to the standard dimensions for a compression test on a Gleeble-3500 thermomechanical simulator, were cut along the rolling direction by wire-electrode cutting. The experimental procedure for fabricating the ultrafine-grained medium-carbon steel is illustrated in Fig. 1a. The cylindrical specimens were first austenitized at 950°C for 20 min followed by quenching to obtain a complete martensitic starting microstructure. Due to the very small amount, the retained austenite is considered to be inexistent and its effects on the mechanical properties and microstructural evolution of deformed martensite are negligible. In some earlier studies [15-17], full martensite starting microstructure after quenching was assumed. Then the martensitic specimens were reheated to 550°C or 650°C with a heating rate of 10°C/s and held for 90 s at the target temperatures, ensuring uniform temperature in specimens. After isothermal holding, warm deformation by 50% reduction in length was obtained with a strain rate of 0.001 s^{-1} to 1 s^{-1}. Finally, all specimens were air cooled to room temperature. The inert gas argon (Ar), in a highly pure form, was filled during the whole process to prevent the oxidation and decarburization of the specimens. In addition, tungsten gaskets were used on the ends of specimens to reduce the friction between the specimens and pressure head and alleviate the inhomogeneous deformation during the compression.

In order to observe the microstructure observation, the cross-section of each specimen was mechanically ground and then polished on a metallographic polishing machine. The specimens were etched with 4% nital. The microstructure was observed on an optical microscope (OM) and a Nova 400 Nano scanning electron microscope (SEM) operated at an accelerating voltage of 20 kV. Energy dispersive spectroscopy (EDS), including point analysis and selected area elemental mapping, was employed to analyze the precipitation compositions. Hardness tests were carried out on an HV-1000 microhardness testing machine with a loading force of 200 g and a loading time of 10 s, and more than five points were measured for the average value of hardness.

3. Results and discussion

3.1. Warm deformation behavior

It is well known that softening due to dynamic recovery (DRV) and recrystallization (DRX) and work-hardening induced by deformation defects concomitantly occur during the warm deformation [19,20]. The true stress-strain curves during warm deformation at different strain rates and temperatures for quenched medium-carbon steel are shown in Fig. 2. It can be observed that the flow stress increased with an increase in strain rate and a decrease in temperature. There were three typical stages in the true stress-strain curves during the warm deformation. At first, flow stress sharply increased with the increasing strain owing to the strong work-hardening. During this stage, the effect of work-hardening was much intensive than the softening effect. With an increasing strain, the softening effect due to the DRV or DRX generally increased and the flow stress reached the peak stress. It was observed that the peak stress increased with the increasing strain rate and the decreasing deformation temperature. Then, after the peak strain (corresponding to peak stress), the flow stress decreased, thus demonstrating that DRV or DRX played a dominant role. Finally, the flow stress was almost stable or slightly fluctuated with the increasing of strain, indicating that a dynamic equilibrium was achieved between the work-hardening and softening.

DRX is a continuous process including nucleation and growth and takes some time to complete. The deformation time decreased from 693.0 s to 69.3 s, 6.93 s, and 0.693 s when the strain rate was increased from 0.001 s^{-1} to 1 s^{-1}. The decrease in flow stress at a low strain rate (0.01 s^{-1} and 0.001 s^{-1}) was mainly caused by the DRX because it took relatively a long time

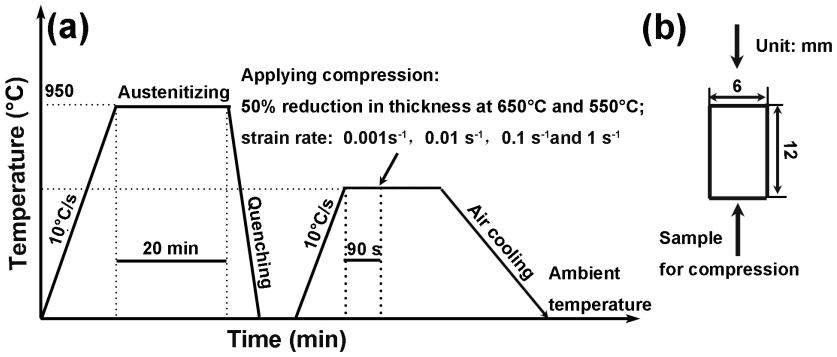

Fig. 1. (a) The experimental procedure and (b) the dimensions of cylindrical specimens used for warm deformation

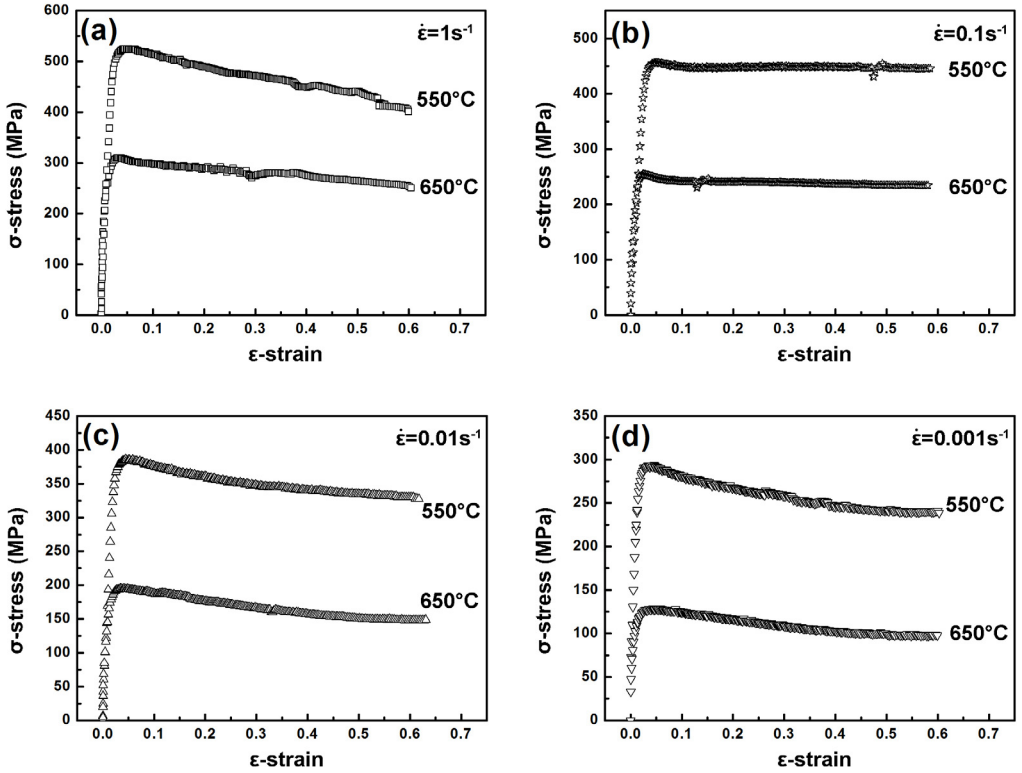

Fig. 2. True stress-strain curves obtained for warm deformation at different strain rates and temperatures in quenched medium-carbon steel

for the deformed martensite to be recrystallized. On the other hand, DRX could not occur because of a short deformation time at a high strain rate of 1 s^{-1} and 0.1 s^{-1}. There was not enough time for the plastic deformation and heating to propagate and the deformation heating was high at a high strain rate due to the fast deformation, thus resulting in a decrease of flow stress after the peak value. Similar results have also been reported earlier [17,21-23]. Whereas the flow stress always increased at a strain rate of 1 s^{-1} with the strain at high-temperature ≥900°C [24]. This discrepancy could be attributed to the different initial microstructure of polygon ferrite and pearlite and a higher deformed temperature in ref. [24].

Fig. 3 displays the microstructures of the specimens deformed at 550°C and strain rate of 1 s^{-1} and 0.001 s^{-1}. It is evident that DRX occurred in the specimen at 550°C and strain rate of 0.001 s^{-1}, whereas no DRX occurred in the specimen at 550°C and strain rate of 1 s^{-1}, confirming with the above discussion and speculation.

According to the equations of dislocation dynamics [25]:

$$\dot{\varepsilon} = \rho b v \tag{1}$$

$$v = A\sigma^m \tag{2}$$

where $\dot{\varepsilon}$ is the strain rate, ρ is the density of activity dislocation, b is burgers vector, v is the average motion rate of dislocation, A is a constant and σ^m is the deformation resistance. It can be observed that the average motion rate of dislocation increases with the increasing strain rate, thus leading to a larger deforma-

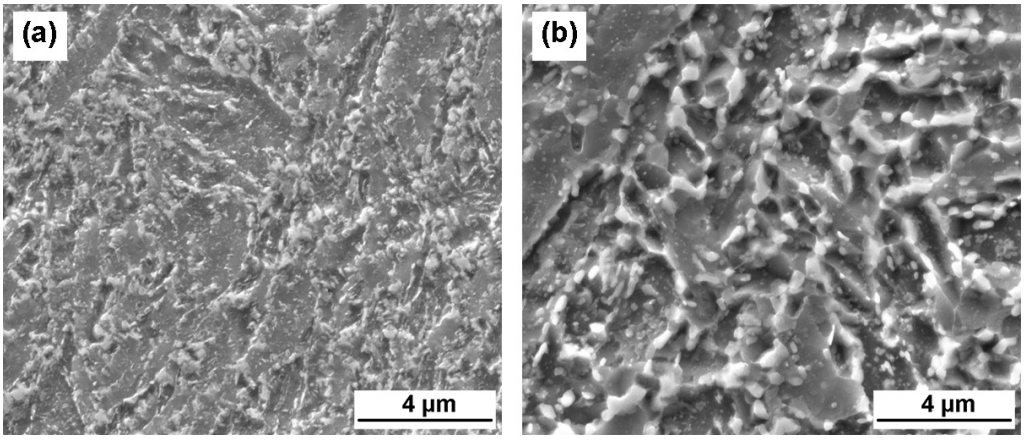

Fig. 3. The microstructure of the specimens deformed at 550°C and strain rate of (a) 1 s^{-1} and (b) 0.001 s^{-1}

tion resistance. Therefore, the flow stress increased with the strain rate.

The reasons behind the decrease in the deformation resistance along with the increasing deformation temperature can be summarized as follows. Firstly, the amplitude of the atomic thermal vibration increases with the increasing deformation temperature during the warm deformation, resulting in an unstable state of atoms in lattice [23]. Thus, the bonding force among the metal atoms is reduced. Secondly, the increase in deformation temperature facilitates the sliding motion of dislocations and the palingenetic sliding systems are continually active, thus reducing the deformation resistance. Thirdly, the DRV or DRX is accelerated at a high deformation temperature, eliminating some work-hardening in materials [26].

It can be noted that the flow stress reached the maximum and decreased sharply after the peak strain for the specimen deformed at 550°C and strain rate of 1 s^{-1}. As mentioned above, the flow stress increased with the increasing strain rate and decreasing deformation temperature. Thus the flow stress reached the maximum value at 550°C and a strain rate of 1 s^{-1}. Moreover, the adiabatic heating induced by the deformation at 550°C and a high strain rate of 1 s^{-1} was comparatively more intense than that occurred at a lower strain rate and a higher deformation temperature, which could be inferred from Eq. (3). This viewpoint is consistent with an earlier work [21]. The temperature rise ΔT in the deformed material can be calculated by Eq. (3) [27]:

$$\int_{T_0}^{T_0+\Delta T} \rho C \mathrm{d}T = \int_{\varepsilon_0}^{\varepsilon_0+\Delta\varepsilon} \sigma \mathrm{d}\varepsilon \Rightarrow \Delta T = \frac{\bar{\sigma}\Delta\varepsilon}{\rho C} \tag{3}$$

where, ρ is the density of material, σ is the true stress, C is the specific heat, $\Delta\varepsilon$ is the interval of the strain and $\bar{\sigma}$ the mean stress. Therefore, ΔT increased with an increasing mean stress and a temperature rise of 550°C and the strain rate of 1 s^{-1} was highest due to the maximum flow stress, resulting in a fast decrease of the stress after the peak value (Fig. 2a).

3.2. Constitutive equation

The constitutive equation of warm deformed medium-carbon martensite can guide the guidance for the optimization of deformation technology to produce ultrafine grains. A hyperbolic-sine function is selected to characterize the relationship between deformation resistance and deformation parameters for total stress range (Eq. 4) [28]:

$$\dot{\varepsilon} = A[\sinh(\alpha\sigma)]^n \exp\left(-\frac{Q}{RT}\right) \tag{4}$$

where, $\dot{\varepsilon}$ is the strain rate, A is material structure constant, α is the parameter of stress level and $\alpha = \beta/n_1$ (β and n_1 are coefficients of stress and strain), σ is peak stress, n is stress exponent, Q is the apparent activation energy of deformation, R is the gas constant and T is deformation temperature (K). The strain rate and deformation temperature are often combined into a Zener-Hollomon parameter Z, which is usually employed to weight the effect of deformation temperature and strain rate on the deformation behavior.

$$Z = \dot{\varepsilon}\exp\left(\frac{Q}{RT}\right) \tag{5}$$

Therefore, the relationship between Z and σ could be signified by Eq. (6) [29]:

$$Z = A\left[\sinh\left(\alpha\sigma\right)\right]^n \tag{6}$$

Then taking the natural logarithm of both sides of Eqs. 4~6, linear equations 7~9 can be obtained as follows:

$$\ln\dot{\varepsilon} = \ln A - \frac{Q}{RT} + n\ln\left[\sinh\left(\alpha\sigma\right)\right] \tag{7}$$

$$\ln\left[\sinh\left(\alpha\sigma\right)\right] = \frac{1}{n}(\ln\dot{\varepsilon} - \ln A) + \frac{Q}{RT}\left(\frac{1}{T}\right) \tag{8}$$

$$\ln Z = \ln A + n\ln\left[\sinh\left(\alpha\sigma\right)\right] \tag{9}$$

In order to improve the accuracy of the calculation, α is determined by the relationship, $\alpha = \beta/n_1$, instead of taking as an empirical constant. The values of β and n_1 were found to be $\beta = 0.033985$ and $n_1 = 9.716805$, showing the relationships between $\ln\dot{\varepsilon}$ and σ, and $\ln\dot{\varepsilon}$ and $\ln\sigma$, respectively (Fig. 4). Therefore, $\alpha = \beta/n_1 = 0.0035$.

The relationships between $\ln\sin h(\alpha\sigma)$ and $\ln\dot{\varepsilon}$, $\ln\sin h(\alpha\sigma)$ and $1000/T$ are illustrated in Fig. 5. According to the linear fit-

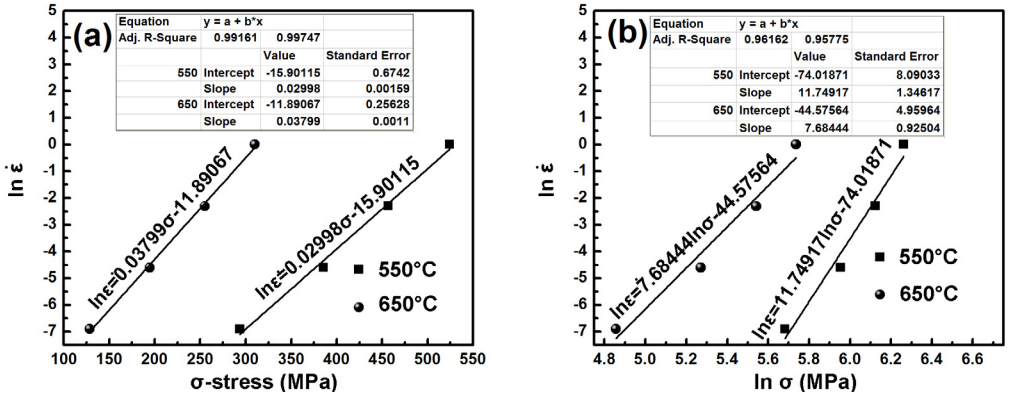

Fig. 4. Relationships between (a) $\ln\dot{\varepsilon}$ and σ, and (b) $\ln\dot{\varepsilon}$ and $\ln\sigma$

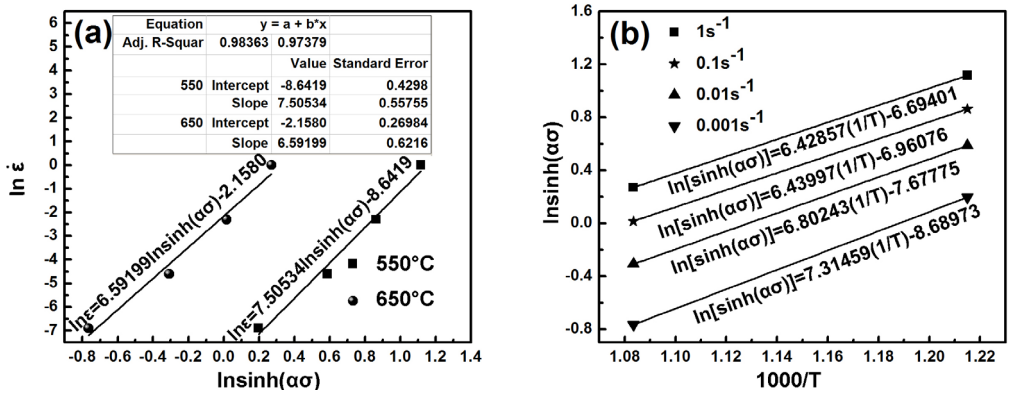

Fig. 5. The relationship between ln$\sin h(\alpha\sigma)$ and (a) $\ln\dot{\varepsilon}$ and (b) $1000/T$

ting, stress exponent n and activation energy Q were calculated to be 7.0487 and 395.17 kJ·mol^{-1}, respectively.

Material structure constant A can be determined by the relationship between ln$Z$ and ln($\sin h(\alpha\sigma)$) as shown as in Fig. 6a. The intercept ln$A$ of the fitting equation was found to be 49.45617, thus A was determined as 3.01×10^{21}. Finally, the constitutive equation of warm deformed medium-carbon martensite could be written as:

$$\dot{\varepsilon} = 3.01\times10^{21}[\sinh(0.0035\sigma)]^{7.0487}\ \exp\left(-\frac{395170}{RT}\right) \quad (10)$$

In addition, the relationship between the strain, stress and the exponent of strain rate sensitivity m is expressed as Eq. (11) [30]:

$$\sigma = A\dot{\varepsilon}^{m} \quad (11)$$

Then m was determined to be 0.083 and 0.126 for the specimens deformed at 550°C and 650°C, respectively (Fig. 6b). It is worth mentioning that the exponent of strain rate sensitivity increased with the deformation temperature, manifesting that the tested medium steel has better ductility at high-temperature deformation.

3.2. Microstructure evolution

The original microstructure of the tested steel is exhibited in Fig. 7a. It can be seen that the microstructure mainly consisted of ferrite (F) and pearlite (P). Ferrite distributed in equiaxed polygon morphology and pearlite with irregular banding shape located adjacent to ferrite. After quenching, complete lath martensite, as shown in Fig. 7b, was obtained in the tested steel. Lath martensite is a suitable microstructure for the grain refinement due to its unique structural features [31,32]. There are three kinds of structure termed as a lath, block, and packet in lath martensite. During quenching, one austenite grain is subdivided into several packets, and several blocks and laths exist in one packet. Conspicuously, there exists an obvious refinement from the packet morphology to lath morphology. In comparison to the original microstructure, lath martensite is thinner in structure. In addition, high-density high-angle boundaries and intricate morphology confer a strong constraint effect during the plastic deformation, resulting in inhomogeneous deformation. Thus, a large amount of misorientation could be obtained in the deformed microstructure. Finally, martensite has a high dislocation density, which can offer a large number of nucleation sites for grain refinement.

The microstructures of the specimens after warm deformation at 550°C and different strain rates are shown in Fig. 8. Compression with a high strain rate of 1 s^{-1} resulted in an apparent deformed microstructure. Distinct lamellar dislocation cell (LDC) and irregularly bent lamellar pattern (IBL) were observed. As to the specimen deformed at 0.01 s^{-1}, some equiaxial ferrite grains and irregular rod-like carbides can be observed, demonstrating the initiation of DRX. With a further decrease in the strain

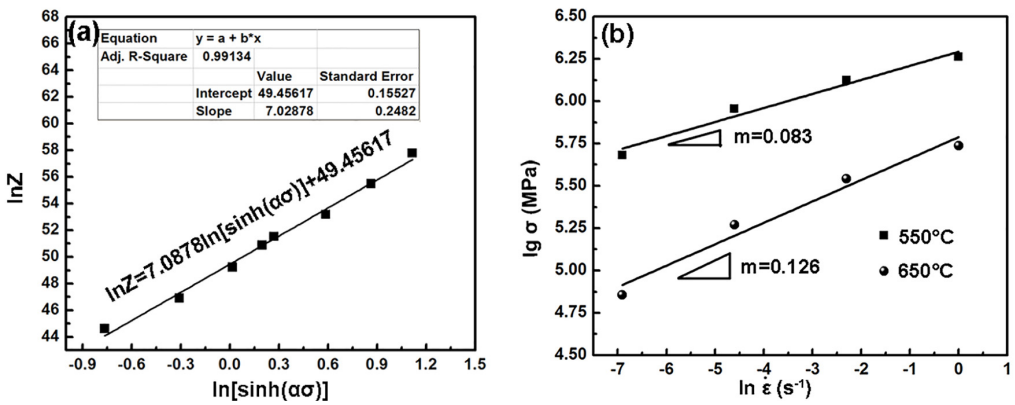

Fig. 6. The relationship between (a) ln$Z$ and ln$\sin h(\alpha\sigma)$, and (b) $\ln\dot{\varepsilon}$ and lgσ

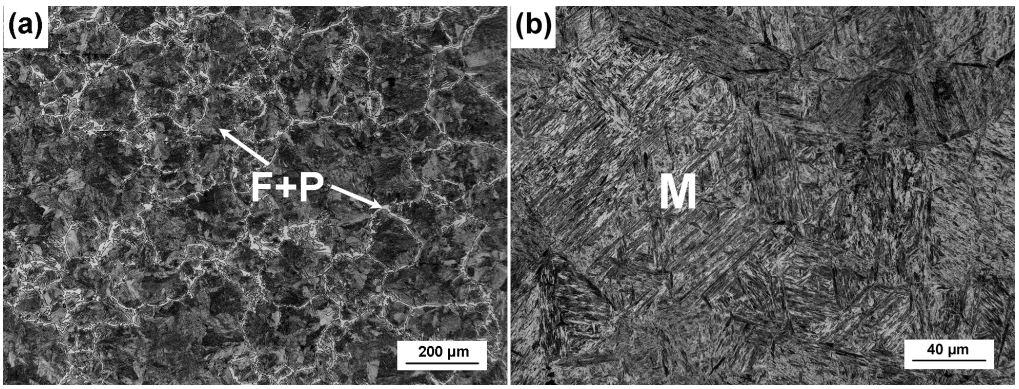

Fig. 7. (a) Original microstructure of the tested steel and (b) quenched martensite

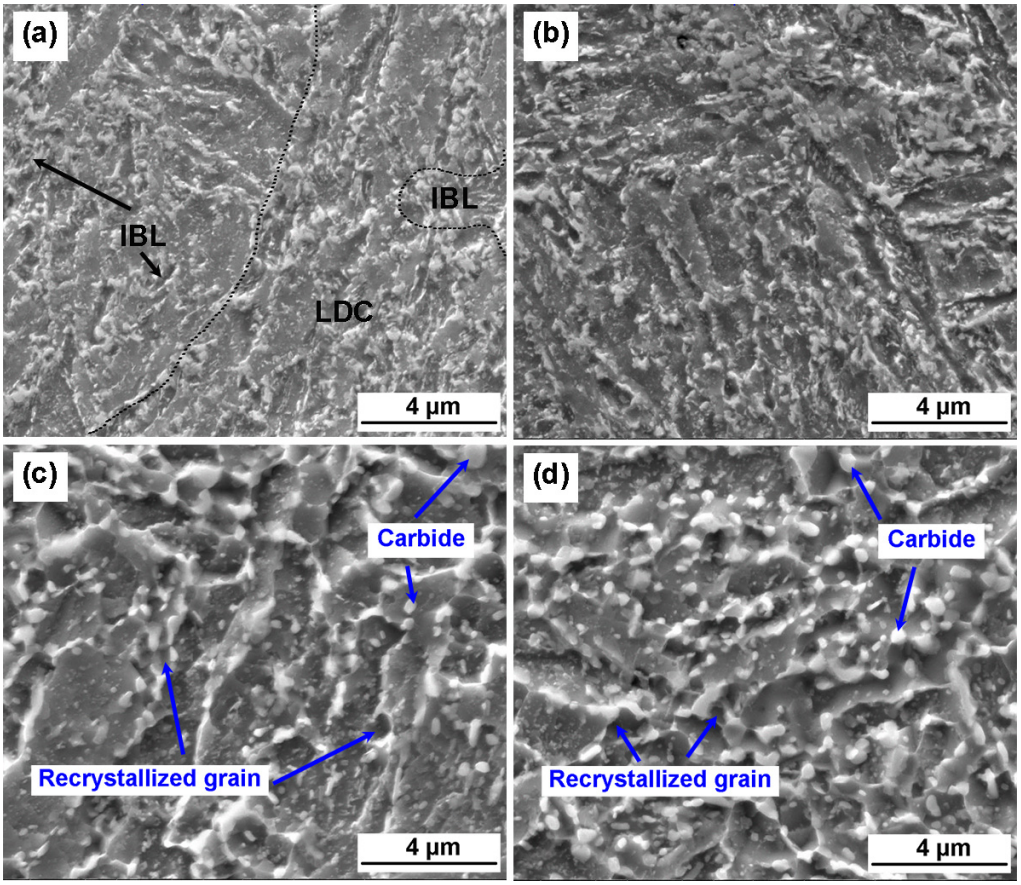

Fig. 8. Microstructures in specimens after warm deformation at 550°C with different strain rates: (a) 1 s^{-1}; (b) 0.1 s^{-1}; (c) 0.01 s^{-1} and (d) 0.001 s^{-1}

rate, equiaxial ferrite grains and spherical carbides appeared. The complete dynamical recrystallization occurred in the specimens deformed at a strain rate of 0.001 s^{-1}. In addition, the spherical carbides were in two dimension ranges. The coarse carbides were mainly distributed at the grain boundaries and trigeminal grain boundaries of the recrystallized ferrite grains, whereas the fine carbides were mainly located in the ferrite grains. The type of carbides was determined by point analysis and the selected-area elemental mapping on EDS as shown in Fig. 9. Only elements Fe and C were detected and the atom ratio of Fe and C was close to 3:1. Thus, the carbides were Fe_3C.

The simplified schematic diagram of the formation of Fe_3C is illustrated in Fig. 10. The precipitation of Fe_3C during the warm deformation is a progressive process, which depends on the oversaturation state and diffusion ability of carbon. The earlier precipitated Fe_3C was formed unceasingly and grew into a rod-like shape due to a favorable crystallographic orientation. The interface energy was higher in Fe_3C with a rod-like shape compared to the spherical carbides, making the rod-like Fe_3C particles to be unstable. Therefore, rod-like Fe_3C in an unstable state would gradually dissolve into spherical Fe_3C particles. This can be explained by two main reasons. On the one hand, high strain storage energy generates during the warm compression, which makes the mass carbon atoms readjust rapidly. On the other hand, the propagated dislocation after deformation can provide more nucleation sites for carbides and diffusion paths for

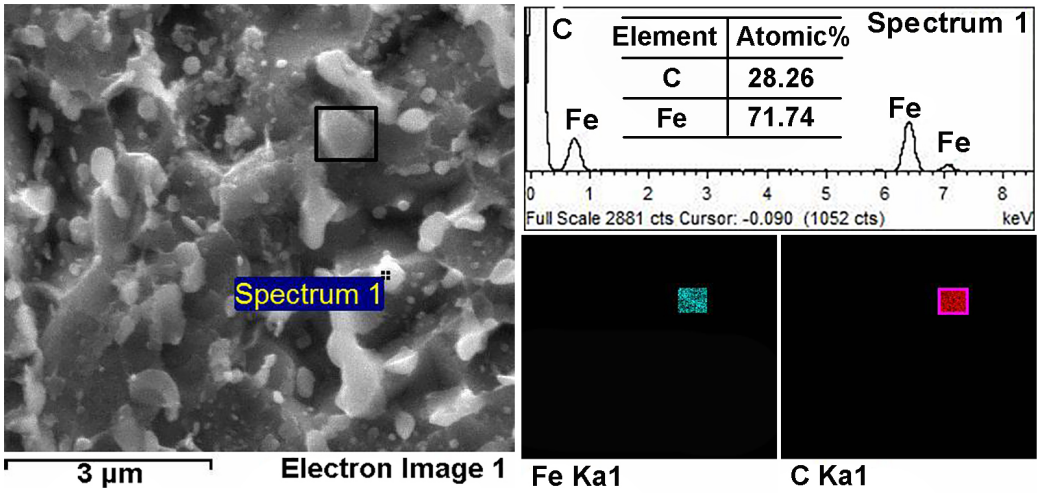

Fig. 9. EDS results indicating Fe_3C precipitates

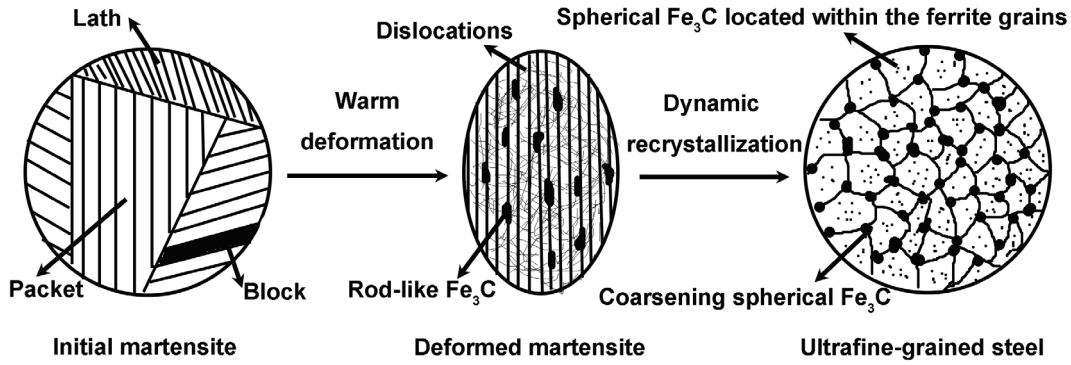

Fig. 10. Schematic diagram of the formation of Fe_3C

carbon atoms. Thus the diffusion of carbon atoms is immensely accelerated under the effect of thermal activation, which is beneficial to the precipitation of spherical Fe_3C. Therefore, Fe_3C particles spontaneously evolve from unstable rod-like Fe_3C to spherical Fe_3C particles. The size of spherical Fe_3C particles depends on the strain rate and temperature. The spherical Fe_3C particles were larger at high temperature and low strain rate. In addition, the coarsening of spherical Fe_3C particles at the boundaries was related to the nonuniform strain storage energy in ferrite grains and at grain boundaries. Fe_3C particles were preferentially formed and aggregated at the grain boundaries due to the higher strain storage energy.

The microstructures of the specimens after warm deformation at 650°C with different strain rates are presented in Fig. 11. DRX initiated in the specimen deformed with a strain rate of 0.1 s^{-1} and some equiaxial ferrite grains and rod-like Fe_3C particles were observed. Different to the completion of DRX in the specimen at 550°C and 0.001 s^{-1}, the DRX accomplished in the specimen deformed at 650°C with a strain rate of 0.01 s^{-1}. The recrystallized ferrite grains grew up at a strain rate of 0.001 s^{-1}. The DRX behavior depends on the deformation temperature and time. With an increase in the deformation temperature, the driving force for DRX increases due to the easier diffusion of atoms. Thus, DRX can accomplish in less time at a higher strain rate. The recrystallized ferrite grains obviously grew up at a strain rate of 0.001 s^{-1} due to longer deformation time of 693 s. However, the size of Fe_3C particles had no apparent change at the strain rates of 0.01 s^{-1} and 0.001 s^{-1}.

The mean linear intercept method (MLIM) was applied to measure the size of recrystallized ferrite grains [33] and the size of Fe_3C particles was measured by the chord-line method. Three images at the same magnification and more than 120 grains (precipitations) were measured to improve the accuracy. As shown in Fig. 12, the size of Fe_3C particles in the specimen formed at 550°C (0.24 ± 0.03 μm) was slightly smaller than that in the specimens at 650°C. Normally, the size of Fe_3C is positively correlated with the diffusion coefficient of carbon atoms, and the diffusion coefficient of carbon increases with the temperature, thus resulting in slightly bigger Fe_3C particles in the specimen at 650°C. Regarding the size of Fe_3C particles at 650 °C, the adiabatic heating at a strain rate of 0.01 s^{-1} was larger (0.36 ± 0.045 μm). On the other hand, deformation time was longer at 0.001 s^{-1} (0.39 ± 0.05 μm), leading to the almost the same size of Fe_3C particles at 650°C.

The size of ferrite grains was obviously increased with the increasing deformation temperature, whereas it only slightly increased with a decrease in the strain rate at 650°C. The DRX was completed in the specimen at 650°C and strain rate of

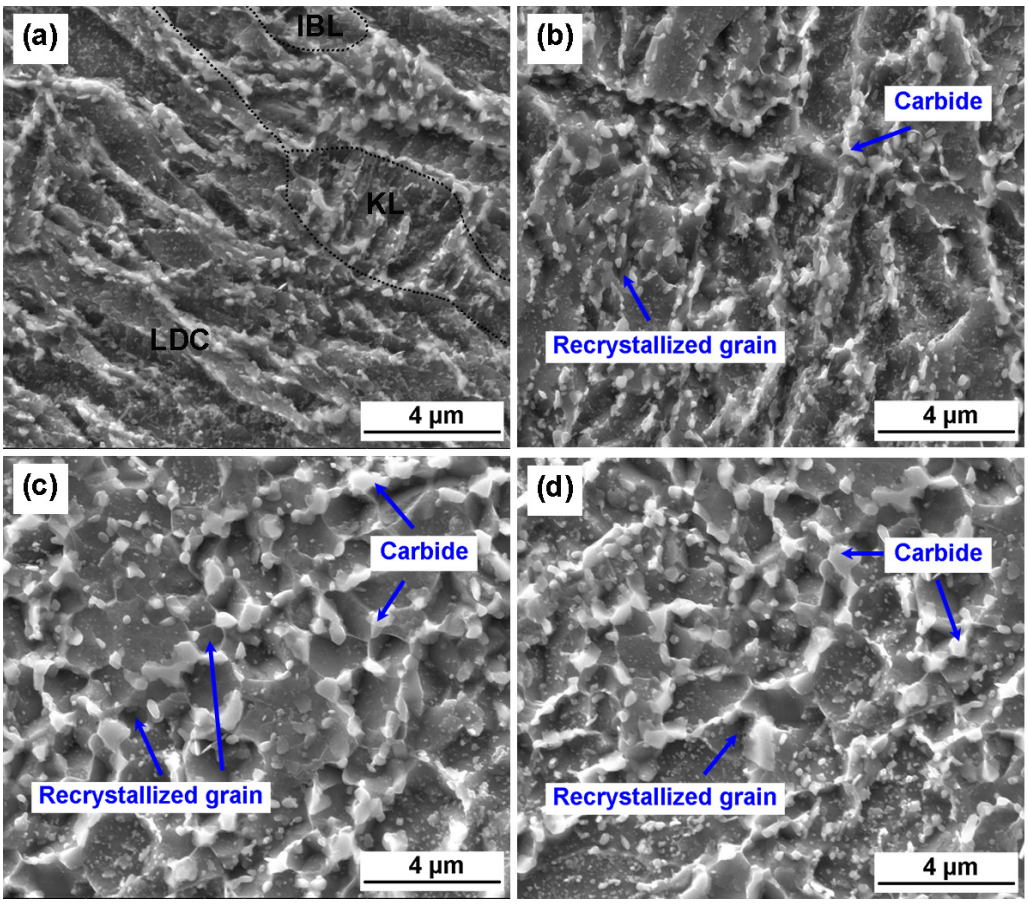

Fig. 11. Microstructures in specimens after warm deformation at 650°C with different strain rates: (a) 1 s^{-1}; (b) 0.1 s^{-1}; (c) 0.01 s^{-1} and (d) 0.001 s^{-1}

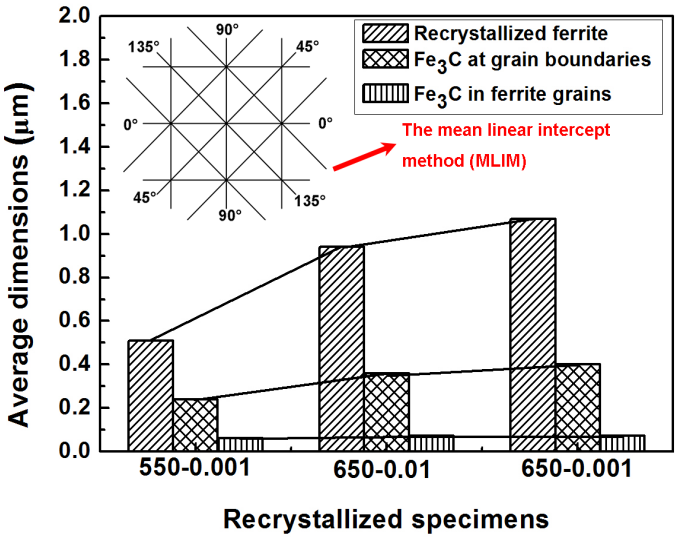

Fig. 12. The size of ferrite grains and Fe_3C particles in completely recrystallized specimens

0.01 s^{-1}, and the average size of ferrite grain was 0.94 ± 0.11 μm. The average ferrite grains grew up to 1.01 ± 0.12 μm in the specimen at 650°C and strain rate of 0.001 s^{-1} due to the longer deformation time.

3.3. Hardness

Hardness tests were conducted to characterize the property of specimens (Table 1). The as-quenched martensite had the maximum hardness of 570.89 Hv due to the refined martensite microstructure. The specimen deformed at 550°C and a strain rate of 0.001 s^{-1} had the maximum hardness compared to other recrystallized specimens. The hardness increased with an increasing strain rate at 650°C and a decreasing deformation temperature from 650°C to 550°C. The increase of hardness was consistent with the size of the ferrite grains.

In summary, ultrafine-grained medium-carbon steel with an average ferrite grain size of 500 ± 58 nm was fabricated by warm deformation at 550°C and a strain rate of 0.001 s^{-1}. The recrystallized ferrite grains grew up at 650°C and a strain rate of 0.001 s^{-1}. Therefore, the suitable deformation condition is important to obtain ultrafine grains in medium-carbon steels.

TABLE 1

The hardness of recrystallized specimens after warm deformation

Specimens	as-quenched	550-0.001	650-0.001	650-0.01
HV	570.89	289.65	250.68	261.66

4. Conclusions

In the current work, warm deformation behavior and carbide precipitation in medium-carbon steel at two temperatures and four strain rates were analyzed. The following conclusions can be drawn:

(1) Ultrafine ferrite grains of an average size of 500 ± 58 nm were obtained by warm deformation at 550°C and strain rate of 0.001 s^{-1} in medium-carbon steel.

(2) The size of Fe_3C was slightly decreased with a decrease in the deformation temperature. The strain rate had no apparent effect on the size of Fe_3C particles.

(3) The exponent of strain rate sensitivity increased with the deformation temperature. The complete recrystallization occurred at a higher strain rate with the increasing temperature.

(4) The constitutive equation of warm deformed martensite for the tested medium-carbon steel could be proposed as:

$$\dot{\varepsilon} = 3.01\times10^{21}[\sinh(0.0035\sigma)]^{7.0487}\ \exp\left(-\frac{395170}{RT}\right) \quad (12)$$

Acknowledgments

The authors gratefully acknowledge the financial supports from The Major Projects of Technology Innovation of Hubei Province (2017AAA116), the National Natural Science Foundation of China (NSFC) (No. 51274154), the National Nature Science Foundation of China (No.51704217) and Hebei Joint Research Fund for Iron and Steel (E2018318013).

REFERENCES

[1] K. Lu, Sci. **345**, 1455-1457 (2014).

[2] B.F. Wang, J.Y. Sun, J.D. Zou, S. Vincent, J. Li, J. Cent South Univ. **22**, 3698-3074 (2015).

[3] K. Matsybara, Y. Miyahara, Z. Horita, T.G. Langdon, Acta Mater. **51**, 3073-3084 (2003).

[4] D.H. Shin, B.C. Kim, K. Park, Y.S. Kim, Acta Mater. **48**, 2247-2255 (2000).

[5] N. Tsuji, K. Shiotsuki, Y. Saito, Mater Trans JIM. **40**, 765-771 (1999).

[6] N. Tsuji, R. Ueji, Y. Saito, Mater. Jpn. **39**, 961-970 (2000) (in Japanese).

[7] Y. Saito, H. Utsunomiya, N. Tsuji, T. Sakai, Acta Mater. **47**, 579-583 (1999).

[8] A. Belyakov, Y. Sakika, T. Hara, Y. Kimura, K. Tsuzaki, Metall. Mater Trans A. **34**, 131-138 (2003).

[9] S. Takaki, K. Kawasaki, Y. Kimura, Ultrafine grained materials. In: Mishra, R.S. (eds.) The Minerals, Metals & Materials Society (TMS), 247-255, Warrendale 2000.

[10] R.Z. Valiev, Y. Ivanisenko, E.F. Rauch, B. Baudelet, J. Mater. Sci. **47**, 7789-7795 (2012).

[11] Z. Horita, D. Smith, M. Furukwa, M. Nnemoto, R.Z. Valiev, T.G. Langdon, J. Mater. Res. **11**, 1880-1890 (1996).

[12] N. Tsuji, R. Ueji, Y. Minamino, Y. Saito, Scripta Mater. **46**, 305-310 (2002).

[13] R. Ueji, N. Tsuji, Y. Minamino, Y. Koizumi, Acta Mater. **50**, 4177-4189 (2002).

[14] J.P. Masse, B. Chehab, H. Zurob, D. Embury, X. Wang, O. Bouaziz, ISIJ Int. **54**, 235-239 (2014).

[15] X. Zhao, Advanced Materials Research, Trans Tech Publications, 853-856, Switzerland 2008.

[16] K. Hase, N. Tsuji, Scripta Mater. **65**, 404-407 (2011).

[17] Q. Li, T.S. Wang, T.F. Jing, Y.W. Gao, J.F. Zhou, J.K. Yua, H.B. Li, Mater. Sci. Eng. A. **515**, 38-42 (2009).

[18] C. Ruffing, Y. Ivanisenko, E. Kerscher, 6th International Conference on Nanomaterials by Severe Plastic Deformation, IOP Publishing Ltd, Metz 2014.

[19] J.M. Wang, Y. Zhao, K.S. Cheng, L. Wan, Applied Mechanics and Materials, Trans Tech Publications, 74-79, Switzerland 2014.

[20] Y. Kimura, T. Inoue, Metall. Mater. Trans. A. **44A**, 560-576 (2013).

[21] G. Luo, J. Wu, J. Fan, H. Shi, Y. Lin, J. Zhang, Mater. Sci. Eng. A. **379**, 302-307 (2004).

[22] Q. Li. Warm deformation behavior of quenched carbon steels and the microstructure evolution as well as properties. Dissertation. 2009. (In Chinese).

[23] Y. Han, S. Yan, B.G. Yin, H.J. Li, X. Ran, Vacuum. **148**, 78-87 (2018).

[24] X.R. Lei, Q.F. Ding, Y.Y. Chen, X.L. Rui, J. Iron Steel Res. Int. **20**, 38-44 (2013).

[25] Y.Y. Zong, D.B. Shan, M. Xu, Y. Lv, J. Mater. Process. Technol. **209**, 1988-1994 (2009).

[26] P.J. Wray, Metall. Trans. A **13**, 125-134 (1982).

[27] R. Kapoor, S. Nemat-Nasser, Mech. Mater. **27**, 1-12 (1998).

[28] C.M. Sellars, W.J. Mctegart, Acta. Mater. **14**, 1136-1138 (1966).

[29] K.P. Rao, Y.K.D.V. Prasad, E.B. Hawbolt, J. Mater. Process. Technol. **56**, 897-907 (1996).

[30] V.N. Perevezentsev, V.N. Chuvildeev, S.A. Larin, Superplasticity in Adv. Mater. **5**, 613-618 (1994).

[31] J.Y. Tian, G. Xu, W.C. Liang, Q. Yuan, Metallogr. Microstruct. Anal. **6**, 233-239 (2017).

[32] Q. Yuan, G. Xu, J.Y. Tian, W.C. Liang, Arab. J. Sci. Eng. **42**, 4771-4779 (2017).

[33] Q. Yuan, G. Xu, S. Liu, M. Liu, H.J. Hu, G.Q. Li, Metals. **8**, 518-533 (2018).